Compact, High-Performance Positive Magnetophoresis Chip With Integrated Patterned Magnet for Efficient Particle Trapping

Vinit Kumar Yadav, *Student Member, IEEE*, Yogesh M. Patel, Supreet Singh Bahga, Samaresh Das, and Dhiman Mallick, *Member, IEEE*

***Abstract*— In this work, we demonstrate a cost-effective, scalable, and rapid technique to fabricate a robust, high-performance on-chip positive magnetophoretic system. The system incorporates a thick patterned permanent magnet and microfluidic channel on a single polymethyl methacrylate (PMMA) substrate for on-chip manipulation of magnetic particles (MPs). Using the suitable patterning of the magnet, a spatially varying magnetic force is exerted onto the MPs in the channel, which is pertinent for capturing the MPs at specific locations. The device geometry is optimized using FEM simulations to prevent any blockage in the channel due to the accumulation of the MPs and ease the fabrication process. The ∼1.5-fold enhancement in the trapping efficiency is observed upon lowering the flow rate from 15 μl/min to 9 μl/min, leading to 94.5% trapping efficiency at a lower flow rate of 9 μl/min. [2022-0173]**

***Index Terms*— Permanent magnet, NdFeB, magnetic particle, magnetophoresis, PMMA, PDMS, microfluidics.**

I. Introduction

EFFICIENT trapping and separation of specific biomolecules are critical for reliable and repeatable outcomes of biomedical diagnosis and therapeutic applications [1], [2]. Recently, magnetic micro/nano particles are being utilized as carriers in biological applications as they can efficiently get attached to the desired biological entities due to their superparamagnetic nature, small size, and ease of controlled transport. The rapid advancement of microfluidics has provided a potent tool for transporting magnetically tagged biological samples at targeted locations, as concentrating particles or cells are frequently required in a wide range of chemical and biological applications [3].

Manuscript received 25 September 2022; revised 2 December 2022; accepted 3 January 2023. Date of publication 20 January 2023; date of current version 4 April 2023. This work was supported by the International Bilateral Corporation Division of Department of Science and Technology (DST), Government of India, under Indo-Norway Joint Project, under Project INT/NOR/RCN/NS/P-06/2019. Subject Editor H. Jiang. *(Corresponding author: Dhiman Mallick.)*

Vinit Kumar Yadav and Dhiman Mallick are with the Department of Electrical Engineering, IIT Delhi, New Delhi 110016, India (e-mail: vinit.kumar.yadav@ee.iitd,ac.in; dhiman.mallick@ee.iitd.ac.in).

Yogesh M. Patel and Supreet Singh Bahga are with the Department of Mechanical Engineering IIT Delhi, New Delhi 110016, India (e-mail: mez188261@mech.iitd.ac.in; bahga@mech.iitd.ac.in).

Samaresh Das is with the Centre of Applied Research in Electronics, IIT Delhi, New Delhi 110016, India (e-mail: samaresh.das@care.iitd.ac.in).

Color versions of one or more figures in this article are available at https://doi.org/10.1109/JMEMS.2023.3234760.

Digital Object Identifier 10.1109/JMEMS.2023.3234760

Magnetophoresis, particle migration in a fluidic medium under an external magnetic field, is attractive over other active methods, like electrophoresis, thermophoresis, and acoustophoresis, to manipulate such entities due to its zero-power requirement, low-cost and simple design [4], [5]. Typically, magnetophoresis is classified into two distinct categories, i.e., positive and negative. The movement of magnetic particles in a diamagnetic fluid media is termed as positive magnetophoresis, whereas negative magnetophoresis refers to the movement of diamagnetic particles in a magnetic fluid media. MPs floating in a fluidic media will migrate towards either the maxima or minima of the gradient of the magnetic field [6]. For providing external magnetic field, a permanent magnet or an electromagnet might be employed. The field of permanent magnet based magnetophoresis is attractive due to its noninvasive contactless nature, electrical neutrality, and unaltered sample properties (pH value, surface charge) [7]. Though permanent magnets are energy efficient, they are not efficient as a source of magnetic field when the size scales down as the stray magnetic field appears only from the edge of the magnet, and a large part of the material is wasted [8]. This is due to the presence of the shape-dependent demagnetization field that acts to demagnetize the magnet in opposite direction of the magnetization, reducing the overall magnetic flux density. The above-mentioned problem can be tackled by using miniaturized array or micro-magnetic patterns of permanent magnets such as NdFeB, which can enhance the magnetic field gradient by several orders of magnitude [9], [10], [11]. However, development of thick permanent magnets with desired properties over large area using conventional processes is challenging in terms of time and cost. On the other hand, polymer bonded permanent magnetic powders exhibit magnetic performances comparable to their fully dense counterparts.

Bio-microfluidics applications like trapping, tracing and separation of magnetically tagged biomolecules are of great interest [12], [13], [14], [15]. However, a large magnetic field gradient is necessary to implement that, which mandates the use of a non-uniform magnetic field. A bulk magnet placed near the microfluidic device can provide a quasi-uniform magnetic field that magnetizes the particles or fluid without causing a rapidly changing force to operate on them. Therefore, one major challenge in the efficient design of an on-chip

magnetophoresis device is to integrate thick, high-flux-gradient magnetic structures commensurate with the channel dimensions, which are needed to exert the required magnetic force for manipulating micro/nano particle.

In earlier works, various arrangements of permanent magnets close to the microfluidic channel are organized to capture or separate magnetic particles [5], [16]. Even though such an approach is convenient and easy, maintaining a very close distance between the magnet and channel is quite challenging during the experiment. Reducing the gap between the microfluidic channel and magnet can provide significantly high magnetic field gradient throughout the channel. *Mao* et al. demonstrated four bulk permanent magnets in a quadrupole configuration close to the fluidic channel to obtain a magnetic field gradient of 1.27 kT/m for sorting nanoparticles [17]. Such a type of magnet provides a strong and quasi uniform field distribution throughout the channel, making it difficult to achieve high intensity peaks of magnetic field gradient intermittently for targeting the MPs. In order to enhance magnetic field gradient, the authors described a novel approach to integrate NdFeB based patterned magnets in proximity to the microfluidic channel. *Zhou* et al. described a technique to fabricate patterned micromagnet and microfluidic channel on polydimethylsiloxane (PDMS) followed by soft lithography steps, which allowed to generate a maximum 15 pN force for manipulating the MPs in the microfluidic channel [18]. Zeng et al. demonstrated an on-chip magnetic pole array in PDMS to generate an ultra-high magnetic field gradient of 10^5T/m to separate 0.2 μm and 1 μm magnetic particles using negative magnetophoresis [19]. The preceding literature investigations reveal that high field gradient over a small length scale can boost the magnetic force and thereby enables the particle trapping in a highly localized manner. Using conventional deposition methods, like sputtering, electroplating, and PLD, the deposition thickness of permanent magnets is restricted up to tens to hundreds of microns [11]. Consequently, the limited size often results in a lower magnetic field gradient [5]. On the other hand, cavity filling by magnetic powder using a doctor blade is the conventional method for fabricating high aspect ratio (thickness up to mm range) permanent magnets in MEMS [21], [26]. The magnetization of the filled magnetic composites is proportional to the powder fill factor and as long as the fill factor remains unchanged, magnetic performance remains the same. However, such on-chip cavity filling technique includes corrosive chemical etching and complicated lithography steps in stringently controlled cleanroom to avoid contamination, which consumes prolonged development time. This indicates that there is further scope in terms of realizing simple, low-cost and faster fabrication processes, which makes it convenient to re-use the chip by modifying the magnetic field for alternative applications.

This work demonstrates a simple and novel strategy to fabricate structures for patterned magnet and microfluidic channel on a single PMMA substrate. The current fabrication methodology excludes lithography, etching, or a deposition process and offers several advantages over previously reported techniques, including simple and rapid fabrication techniques,

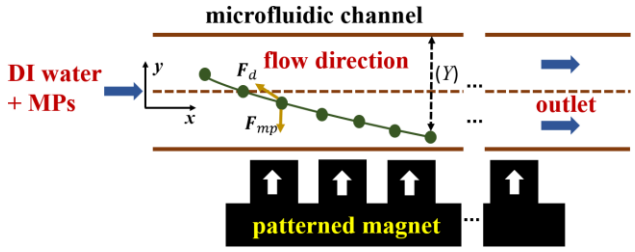

Fig. 1. Schematic representation of positive magnetophoresis, magnetic particles flowing in non-magnetic fluid which attracts towards maxima of magnetic field gradient with deflection (Y) from the upper wall of the channel. Mainly two forces acted on MPs are drag force ($\boldsymbol{F}_d$) due to fluid and magnetic force ($\boldsymbol{F}_{mp}$) due to magnet in a particular direction.

and lowered cost. Before fabricating the device, optimization of the patterned magnet with the microfluidic channel is performed using FEM simulation in COMSOL Multiphysics. Iron oxide (Fe_3O_4) paramagnetic particles of 0.5μm in diameter are then successfully trapped in the magnetophoretic chip by positive magnetophoresis. Compared to the state-of-the-art works on positive magnetophoresis for trapping of MPs, the proposed design of the magnetic structure is arranged in a comparatively thick array with optimized dimensions, leading to a high magnetic field gradient and a larger field intensity. Also, the microfluidic channel is placed at an gap value where the injected particles experiences larger magnetic force (~1.7 times higher than other reported works) which is suitable for effective trapping with enhanced trapping efficiency [17], [18], [20].

II. Design Methodology

A. Working Principle

The mechanism of magnetophoresis refers to the deflection of MPs from the direction of the fluid flow (laminar, incompressible) under an applied magnetic field based on their magnetic susceptibility, shape, and fluid velocity in a continuous flow. In a magnetophoresis device, particles are subjected to several forces, including magnetic, drag, gravitational, and buoyancy forces, which influence the dynamical behavior of the particles. Figure 1 illustrates the phenomenon of positive magnetophoresis. Here, MPs are injected from the inlet in a non-magnetic fluid medium in the presence of an inhomogeneous magnetic field and get deflected (Y) towards the maxima of the magnetic field gradient. The deflection allows to trap MPs at the lower wall of the channel and restrict their motion in the channel. The following equation is used to predict the transport behavior of MPs during magnetophoresis [19].

$$m_{pr}\frac{d\boldsymbol{v}_{pr}}{dt} = \boldsymbol{F}_{mp} + \boldsymbol{F}_d \tag{1}$$

where m_{pr} and $\boldsymbol{v}_{pr}$ are the mass and the velocity of the MPs, while $\boldsymbol{F}_{mp}$ and $\boldsymbol{F}_d$ are magnetic and drag forces, respectively.

Other forces like gravity ($F_g = \rho\left(\frac{4}{3}\right)\pi R_{pr}^3 g$; MP's radius $R_{pr} = 0.25\mu$m, MP's density $\rho = 4800$ kg/m^3, $g = 9.8$ m/s^2) and buoyancy ($F_b = \rho_f\left(\frac{4}{3}\right)\pi R_{pr}^3 g$; fluid density

TABLE I
DESIGN PARAMETER OF THE MAGNETOPHORESIS CHIP

Parameters	Values [μm]
Length of the microfluidic channel (L)	30×10^3
Width of the microfluidic channel (W)	500
Gap between channel & magnet (g)	250
Length of the patterned magnet (l_m)	16.5×10^3
Height of each pattern (h_m)	2000
Width of each pattern (w_m)	2000
Gap between consecutive patterns (g_m)	500

$\rho_f = 1000$ kg/m^3) for Fe_3O_4 particles in water are 4.2×10^{-3}pN and 1.92×10^{-3}pN respectively, which are smaller by many orders than the $\boldsymbol{F}_{mp}$ and $\boldsymbol{F}_d$. Hence, only magnetic and fluidic forces are used in the calculations [20].

$$\boldsymbol{F}_{mp} = \mu_0 V_p \Delta\chi \left(\boldsymbol{H_{ad}} \cdot \nabla\right) \boldsymbol{H_{ad}} \tag{2}$$

where μ_0 is the magnetic permeability of free space, $\boldsymbol{H_{ad}}$ is the applied magnetic field intensity to the particle, $\Delta\chi$ and V_p are the effective magnetic susceptibility and the volume of the MP, respectively.

$$\boldsymbol{F}_d = -6\pi\eta R_{pr}\left(\boldsymbol{v_{pr}} - \boldsymbol{u}\right) \tag{3}$$

where η and $\boldsymbol{u}$ are the dynamic viscosity (0.001 Pa·s) and velocity of the fluid, respectively, and R_{pr} is the radius of the MP. After putting the values of forces ($\boldsymbol{F}_{mp}$ and $\boldsymbol{F}_d$), Equation 1 becomes:

$$m_{pr}\frac{d\boldsymbol{v_{pr}}}{dt} = \mu_0 V_p \Delta\chi \left(\boldsymbol{H_{ad}} \cdot \nabla\right) \boldsymbol{H_{ad}} - 6\pi\eta R_{pr}\left(\boldsymbol{v_{pr}} - \boldsymbol{u}\right) \tag{4}$$

The velocity of the MPs as a function of the applied magnetic field in a pressure driven flow can be determined by solving equation (4) to trace the particle trajectory.

B. FEM Simulation

The design parameters of the proposed magnetophoretic device are mentioned in Table I. The trajectory of MPs in the microfluidic channel at different flow rates (Q) is determined using two-dimensional (2D) modeling in COMSOL Multiphysics before the experimentation (Figure 4). The FEM model consists of mainly three physical domains: laminar flow (incompressible Navier-Stokes), particle tracing for fluid flow, and magnetic field (Magnetic vector potential) module to study the dynamic behaviour of MPs. A free triangular mesh is used with a minimum dimension of 3 μm, refined in the channel and near the patterned magnet. Initially, laminar flow and magnetic field modules are solved by stationary study, afterwards, particle tracing is solved by coupling Navier-stokes and magnetic vector potential in the time-dependent study.

The magnetic field is calculated by solving Maxwell equations ($\boldsymbol{J} = \nabla \times \boldsymbol{H}$ and $\nabla \cdot \boldsymbol{B} = 0$) and magnetic vector potential ($\boldsymbol{B} = \nabla \times \boldsymbol{A}$) in three separate regions: inside the patterned magnet, the channel, and the neighbouring air boundaries. Magnetic insulation condition ($\boldsymbol{A_z} = 0$) is used along the boundary of the system. The inner boundaries of the magnets and the air are assumed to be continuous, corresponding to a congruent Neumann condition. This module obtains the magnetic field parameters, i.e., spatially varying magnetic field intensity, field gradient, and exerted magnetic force on MPs in the microfluidic channel.

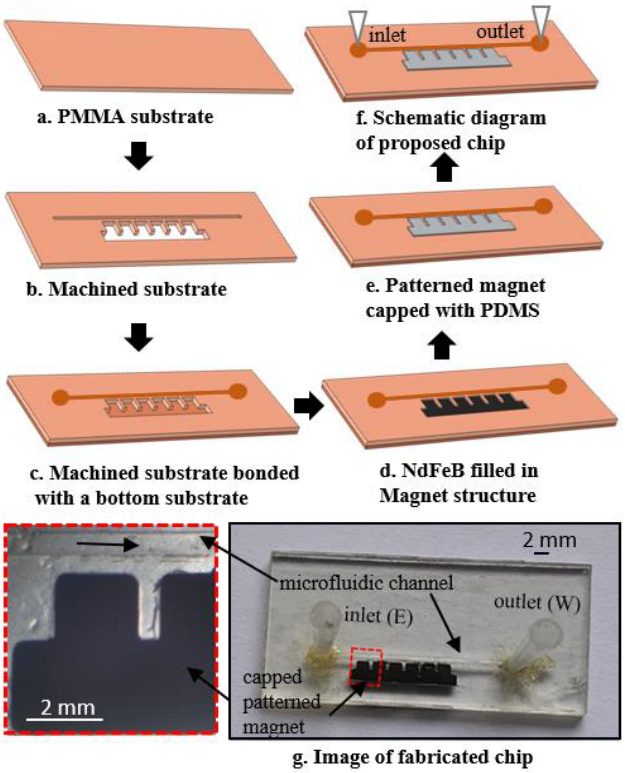

Fig. 2. Fabrication of magnetophoretic chip **(a)** PMMA substrate **(b)** Preparation of structure for magnet, microfluidic channel, and reservoirs **(c)** Structured top substrate sealed with another bottom PMMA substrate by diffusion bonding **(d)** Magnet structure filled with NdFeB (<5μm) powder in the presence of a permanent block magnet to magnetize pattern magnet **(e)** Filled NdFeB is capped with PDMS **(f)** Reservoir are connected with a syringe through pressure monitoring tube, and flow rate of the sample (MPs + DI) is controlled using a syringe pump. **(g)** Photograph of fabricated chip. W and E are the reservoirs for inlet and outlet, respectively. Inset Figure g shows the microscopic zoomed image of the patterned magnet and the microfluidic channel.

The simulation for the particle tracing is performed for four flow rates (Q) 9 μl/min, 15 μl/min, 21 μl/min, 27 μl/min to compare with the experimental results. 6000 MPs are released in the channel and simulated for 100 s with a 0.1 s time interval. To compute the trapping efficiency (TE), which is defined in the following equation (5), the particles at the outlet of the channel are counted using global evaluation ('total number of particles in selection' option) after each simulation [23].

$$TE = \frac{MP_{before\ trapping} - MP_{after\ trapping}}{MP_{before\ trapping}} \tag{5}$$

III. DEVICE FABRICATION AND CHARACTERIZATION

A. Device Fabrication

The device fabrication process flow is shown in Figure 2. The complete magnetophoresis chip is fabricated using two

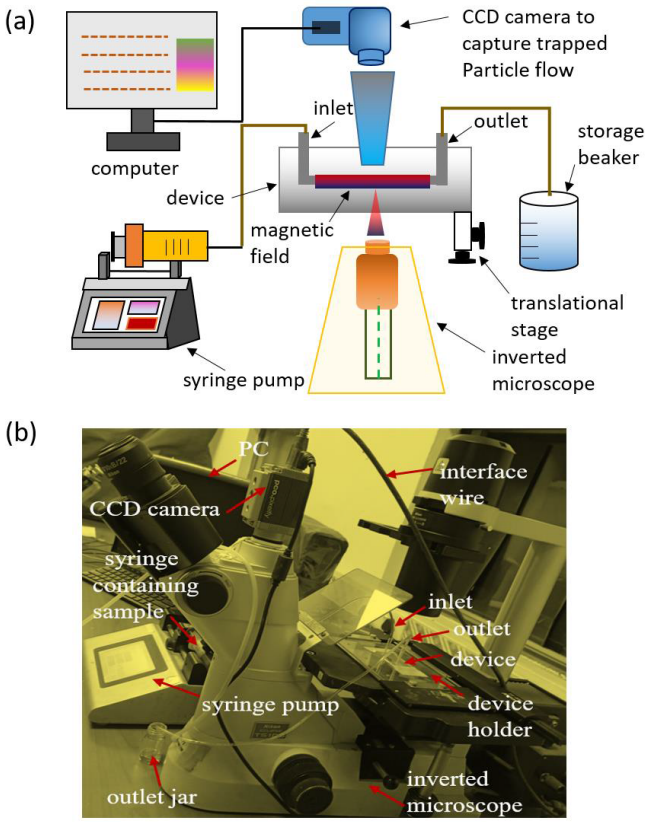

Fig. 3. **(a)** Schematic diagram of the setup to the perform experiment. **(b)** The actual experimental setup.

PMMA substrate; the dimension of the top and bottom substrates are 50 × 25 × 1 mm^3 and 50 × 25 × 3 mm^3, respectively. The structures for the patterned magnet and microfluidic channel are machined on the top substrate using a computer numerical control (CNC) machine with a carbide end mill tool diameter of 500 μm. The depth of the machined patterned structure for the magnet is the same as the depth of the top substrate, i.e., 1000 μm, whereas the depth of the microfluidic channel is 100 μm. The feed rate and spindle speed are kept at 8 mm/rev and 2500 rpm during machining to obtain a good surface finish and avoid tool break-up. The inlet (W) and outlet (E) reservoirs are drilled using the carbide drill tool of diameter 2 mm. The machined top substrate is then cleaned with DI water, IPA, and xylene, and then the open side is thermally bonded with another 3 mm thick PMMA sheet (bottom substrate). The thermal bonding is carried out by clamping both substrates and heating them at 155°C for 25 minutes in a hot air oven. Again, the bonded microfluidic device is cleaned by flowing xylene, IPA, and DI water in the microfluidic channel.

Afterward, the patterned magnet structure is filled with NdFeB magnetic micro-powder (<5μm) using the doctor-blade method [11], [26] in the presence of an external high magnetic field intensity to magnetize the patterned magnets. The top of the filled magnetic surface is capped with PDMS layer to hold the powder in the machined structure. Such embedded capping layer in a robust PMMA substrate gives the patterned magnets application flexibility by allowing it to deactivate or modify the magnetic field strength. Typically, the fabrication of micromagnetic arrays are performed in literature by injecting a composite mixture of NdFeB/PDMS into PDMS structures utilizing MEMS microfabrication method followed by curing, which consists of complex lithography steps, where the deactivation or modification of the magnetic field strength is usually not possible. Here, the PMMA substrate is rigid and compact so that the magnetic powder can be poured directly without any curing agent, and it will not solidify or stick to the machined surface. Therefore, it can be easily washed so that newer magnetic powder can be incorporated into the same chip for altering the field strength on the MPs vis-à-vis improving the reusability of the fabricated chip.

B. Magnetic Powder Characterization

The patterned magnet is prepared using NdFeB powder of 5μm diameter (D50 NCZM125-19), purchased from Nanochemazone. The morphology of the powder is shown in the inset of Figure 5 using Scanning Electron Microscopy (SEM) imaging. In order to find magnetic properties, a sample of 14 gm NdFeB powder is used, which is measured by vibrating sample magnetometer (VSM) module of the physical property measurement system (Quantum Design, PPMS EverCool-II) in the out-of-plane direction with a maximum applied field up to 2400 kA/m (around 3 T).

C. Device Characterization

The sample fluid, consisting of 1g (0.5 μm) Fe_3O_4 particles (susceptibility $\chi_p = 0.2$, Sigma-Aldrich) in 5 ml DI water, is injected from the W reservoir (inlet) by using a syringe pump (Cole Parmer 110 series). The syringe containing the sample is connected to reservoirs using pressure monitoring tubes as shown in the schematic of Figure 3(a). A 1 ml sample is injected for four flow rates 9 μl/min, 15 μl/min, 21 μl/min, and 27 μl/min. Fresh DI water is introduced into the microfluidic channels prior to the commencement of each experiment. The sample stream in the experiments is captured using a 10x objective (CFI Achromat, NA = 0.25) on an inverted microscope (TS100-F, Nikon, Japan), and the data is recorded using a CCD camera and PC/DAQ system (PCO Pixelfly, PCO AG, Germany). Figure 3(b) shows the experimental setup used for characterizations.

IV. Result and Discussion

A. Magnetic Field and Force Analysis

The magnetic hysteresis loop of the utilized NdFeB powder is depicted in Figure 5, which shows intrinsic coercively and saturation magnetization of 350 kA/m and 0.92 T, respectively. The magnetic field intensity and magnetic field gradient due to the patterned magnets are determined using FEM simulation by incorporating the aforementioned measured values from the M-H loop. Before integrating the patterned magnet with the channel, the design parameters of magnet are optimized to obtain the suitable magnetic field intensity and gradient for efficient particle trapping. The gap between two consecutive

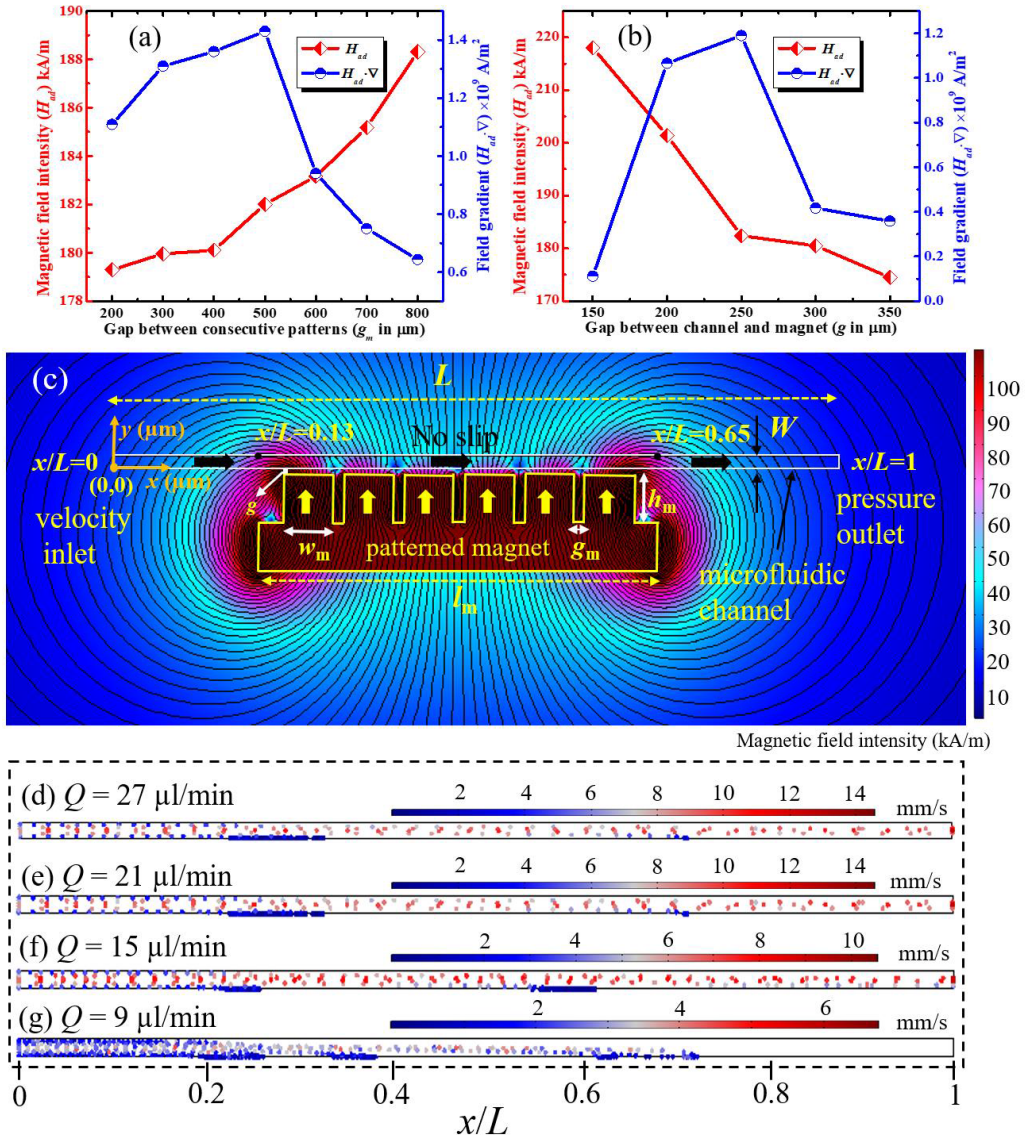

Fig. 4. (a) Maximum magnetic field intensity (line average) and magnetic field gradient with the change in the gap between (a) consecutive patterns (g_m) (b) channel and patterned magnet (g) to optimize patterned magnet parameters with microfluidic channel (c) Simulation of magnetic field intensity (kA/m) due to patterned magnet within the microfluidic channel. Magnetization of the patterned magnet is in the $+y$ *direction*. (d-g) Distribution of MP trapping locations and trajectory in the channel for various flow rates (d) $Q = 27$ μl/min (e) $Q = 21$ μl/min (f) $Q = 15$ μl/min (g) $Q = 9$ μl/min. Color bars in d-g show the velocity of the MPs.

magnets (g_m) is varied from 200 to 800 μm, and the corresponding field intensity and field gradient are measured at a constant height (250 μm), illustrated in Figure 4(a). The result shows that a smaller gap between two consecutive patterns results in significant magnetic field cancellation, thus obtaining a weak magnetic field. Meanwhile, at a particular gap of 500 μm, a rapid change in magnetic field intensity over a short distance is achieved, which leads to a high magnetic field gradient (Figure 4(a)). On the other hand, placing a magnet closer to the channel creates a strong magnetic field but a variable field gradient, whereas putting it further away reduces the strength of the magnetic field. Therefore, the gap (g) between the patterned magnet and the microfluidic channel is further optimized to achieve the highest field gradient, i.e., obtained at $g = 250$ μm, as illustrated in Figure 4(b). Magnetic field strength reduces with the increase in the gap (g) from 150-350 μm, whereas below and above the gap of 250 μm, the rate of change in magnetic field intensity over the distance is minimal. Consequently, the magnetic field gradient increases as the gap increases from 150-250 μm and further decreases as the gap increases from 250-350 μm. Therefore, patterned magnetic structure with $g_m = 500$ μm and $g = 250$ μm is integrated with the microfluidic channel, which is comparatively easier to fabricate and results in a suitable magnetic force to trap the MPs. Nevertheless, a shorter distance from the microfluidic channel leads to the issue of complex fabrication processes. The magnetic field distribution inside the microfluidic channel after integrating the optimized patterned magnets is shown in Figure 4(c). The magnetic pole orientation is expected to impact the magnetic field gradient, which in turn affects the magnetic forces on MPs and their trajectory. For designing the proposed device, the patterned

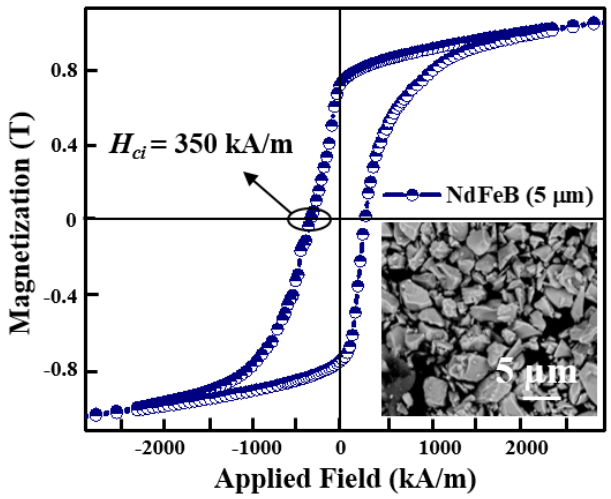

Fig. 5. Magnetization curve of NdFeB powder (5 μm) at room temperature. Inset Figure shows the SEM image of the same.

magnets are initially magnetized along the *y-direction* by using an external magnetic field of 2.5 T. As shown in Figure 4(c), a drastic change in magnetic field intensity is observed laterally inside the microfluidic channel, due to the patterning of the magnets with largest intensities at the extreme edges, i.e., at $x/L = 0.13$ and $x/L = 0.63$, respectively. The upper wall of the microfluidic channel experiences a comparatively weak field intensity, while a consistent enhancement in the intensity is observed up to the bottom wall of the channel, as expected. Further analysis is performed to obtain the magnetic field components at various locations which is shown in Figure 6(a). $\boldsymbol{H_x}$ shows strong intensity at each edge of the pattern and switches signs from one end to another, whereas $\boldsymbol{H_y}$ displays a maximum intensity above the center of each magnetic pattern. In particular, a large spatial variation of the magnetic field component corresponds to a higher magnetic field gradient, which is responsible for a proportional magnetic force exerted on the MPs. The sharp field gradient is observed close to the edge of the magnets, as the maximum change in the field intensity is obtained there. Due to periodic inter-magnet spacing, an inhomogeneous field is created along the channel length, generating alternating field gradient maxima (positive and negative) within the channel [19]. To optimize such alternating zones, FEM simulation of magnetic field gradient in the microfluidic channel for a particular patterned magnet position ($0.38 < x/L < 0.49$) is simulated in the inset of Figure 6(a). It is observed that the magnetic field gradient $\boldsymbol{\partial H/\partial y}$ has a single peak (positive) above the inter-magnet gap spacing within the channel, while $\boldsymbol{\partial H/\partial x}$ has two alternating peaks (positive and negative) at the same location. It should be noted that a high field gradient is formed between two consecutive patterns near the lower wall of the channel and diminishes towards the upper wall. Such type of localized magnetic field gradient is responsible for generating the required magnetic force for trapping the MPs, which can be calculated using equation 2.

The magnetic force acting on the MPs is depicted in Figure 6(b). The net magnetic force experienced by the

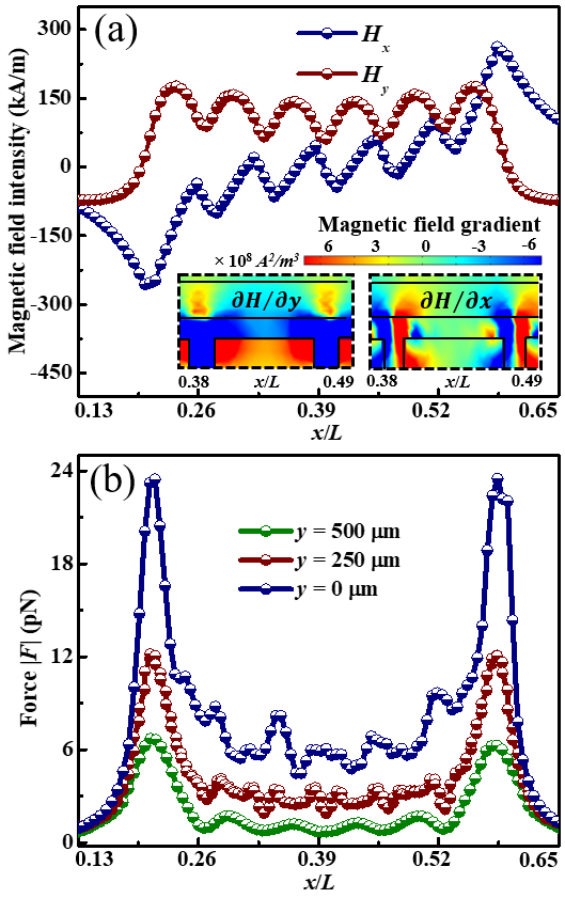

Fig. 6. (a). Magnetic field component ($\boldsymbol{H_x}$ and $\boldsymbol{H_y}$) along the axial direction (*x-direction*) in the microfluidic channel at $y = 250$ μm (middle of the channel width). Inset Figure shows the magnetic field gradient components ($\boldsymbol{\partial H/\partial y}$&$\boldsymbol{\partial H/\partial x}$) above three consecutive patterned magnets in channel for position ($0.38 < x/L < 0.49$) (b). The magnitude of force $|\boldsymbol{F}| = \sqrt{\boldsymbol{F}_{mx}^2 + \boldsymbol{F}_{my}^2}$ (pN) at upper wall ($y = 500$ μm), lower wall ($y = 0$ μm) and middle ($y = 250$ μm) of the channel.

MPs shows an alternating change according to the combined magnitude of the magnetic field intensity and field gradient components. Since the maxima of magnetic force are generally located in the microchannel near the magnet edges, using the designed device, maximum force is generated near the start ($x/L = 0.13$) and end ($x/L = 0.65$) of the pattern magnets similar to the magnetic field gradient variation, according to equation 2. Periodic inter-magnet spacing creates an inhomogeneous field of low intensity between two end points (x/L = 0.13, 0.65) and causes alternating field gradient maxima, resulting in a relatively lower magnetic force. Furthermore, the changes in magnetic force while moving from the lower wall ($y = 0$ μm) to the upper ($y = 500$ μm) wall of the channel width is calculated, which shows the force is maximum at the lower wall and drops consistently till the upper wall of the channel. The maximum magnetic force shows almost two times enhancement at a height of 250 μm from the upper wall of the channel along *-y-direction* and shows around four times increment at the bottom wall with the corresponding values of force being 6.1 pN, 12.2 pN, and 24.4 pN, respectively. The impact of the alternating force on the MP's trajectory is analyzed in the following section.

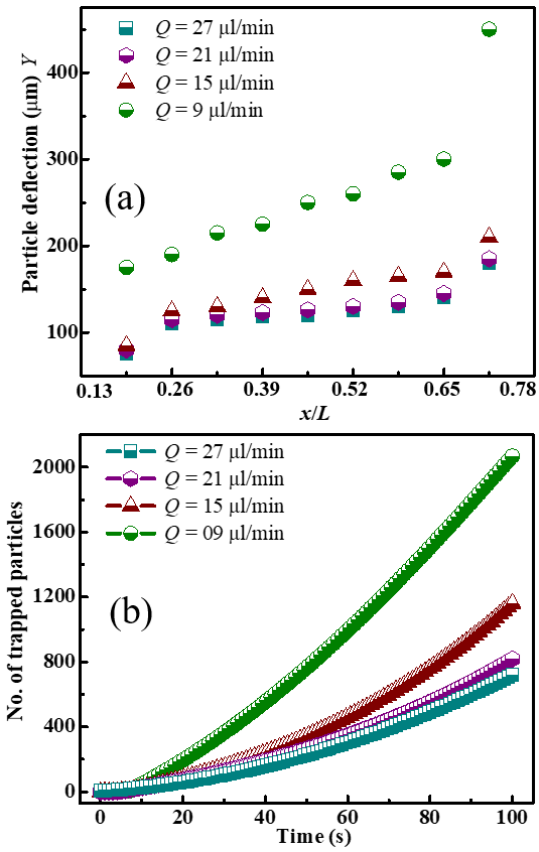

Fig. 7. (a) Particle deflection (Y) along the microfluidic channel length for different flow rates Q = 9-27 μl/min (b) Trapped particles with respect to time (0 - 100 s) and flow rates (Q = 9-27 μl/min).

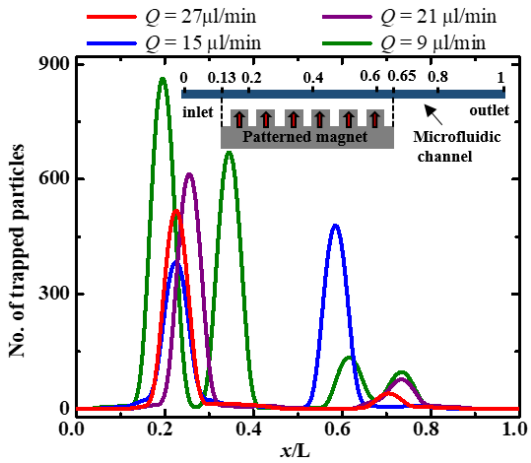

Fig. 8. Trapped particle distribution along microfluidic channel length (0 < x/L < 1) for varying flow rates (Q = 9-27 μl/min).

B. Trajectory and Deflection of the Magnetic Particle in the Microfluidic Channel

To find the trajectory of the MPs, the required boundary conditions and the utilized parameters for numerical simulations are mentioned in Figure 4(c) and Table I, respectively. The trajectory of the MPs is mainly dependent on magnetic force ($\boldsymbol{F}_{mp}$) and drag force ($\boldsymbol{F}_{d}$). Different flow rates, ranging from 9 μl/min to 27 μl/min, are successively introduced from the inlet which corresponds to 2 mm/s to 14 mm/s flow velocity, depicted in Figure 4 (d-g). With the change in the flow rate (Q), the drag force varies according to equation 3, while the magnetic force remains same, as no modifications are, implemented to the patterned magnet or the microfluidic channel parameters. The MPs' laminar flow regime is established in the channel near the inlet, which is visible in the channel region $0 < x/L < 0.13$. This is due to the fact that the strength of magnetic field and corresponding force in this particular region is insignificant to deflect the MPs from its initial flow path. When the MPs reach the active region of the magnet ($x/L \sim 0.13$), they experience alternating magnetic force between the ends of the patterned magnets along the microfluidic channel length, and the MPs deviate from their original path. The velocity of the MPs reduces as the magnetic force is exerted on them, which results in trapping of the MPs at the lower wall of the channel and forms a band of trapped MPs at various locations. Such locations are visualized in Figure 4 (d-g) for different flow rates. Moreover, the width and position of the MP trapping bands depend on the dimension of the microfluidic channel, geometry, strength of the magnetic field, size and susceptibility of the MPs, fluid viscosity and the flow rates etc. In this discussion, all the parameters are fixed except the flow rate Q. Therefore, the MP trapping bands are controlled in the reported compact magnetophoresis device by changing the flow rate for potential applications. Figure 7(a) shows the deflection Y (the position of the MPs from the upper wall of the microfluidic channel) of the MPs while passing the patterned magnet region in the microfluidic channel. It is observed that the deflection of the MP increases continuously as the flow rate decreases, which leads to early trapping of the MPs along the *x-direction* towards the outlet. As there is a trade-off between magnetic and drag forces for manipulating the MPs, the particle behavior (trapping or translating) is decided by the dominating force acting on it. Hence, MPs are not deflected in correspond to the exact maxima position of the magnetic field gradient. Drag force is dominating over the magnetic force for the flow rate ranging from 15 μl/min to 27 μl/min due to higher particle velocity (8 - 14 mm/s). There is a slight change in the deflection along the *y-direction* when the flow rate decreases from Q = 27 μl/min to Q = 15 μl/min (Figure 7(a)). When the flow rate is the lowest, i.e., Q = 9 μl/min, the MPs suspended in the fluidic channel are subjected to a magnetic field gradient for a longer duration, and a significant magnetic force is experienced by the MPs, which strongly dominates the drag force and records a deflection (Y) of ~500 μm. Depending on the deflection of the MPs, the distribution of the trapped particles can be observed in simulated Figure 4 (d-g), which is further verified using experiment for the same flow rates. However, the trapping behavior also changes depending on the particle size; smaller MPs may cause particle trapping to be more dispersed over the bottom wall of the channel, and overall efficiency may decrease [25]. In contrast, trapping locations may be severely limited to fewer locations and trapped relatively near the inlet for the larger-size particles, when using same magnetophoresis device, as shown in Figure 9. The trapping regions are relatively large for different particle types/flow

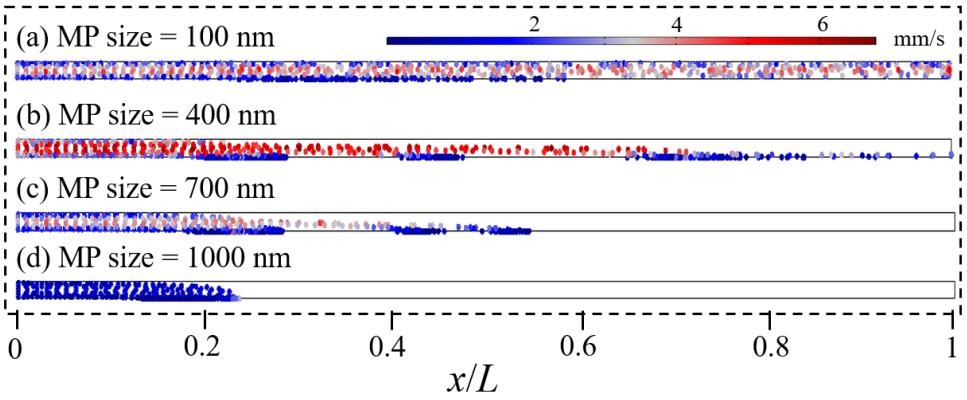

Fig. 9. Distribution of MPs trapping locations and trajectory in the channel for various particle sizes (a) 100 nm (b) 400 nm (c) 700 nm (d) 1000 nm at a similar flow rate of $Q = 9$ μl/min. Color bar shows the velocity of the MPs.

rates and appear to overlap. A bifurcating channel to deflect the particles to an entirely different region downstream can be used to address this issue, which is, however, out of scope for the present study. Moreover, when a mixture of magnetic particles (100-1000 nm) is injected into the device, an effective separation can be enabled by adding two more symmetrical sheath inlets [27] to focus all types of particles in a streamline. Due to the similar magnetic field developing across the streamline, the different-sized particles deflect from a distinct region, which can be efficiently separated using bifurcating channels.

C. Magnetic Particle Trapping Rate and Trapping Distribution

Furthermore, trapping rates for the MPs are studied in this section to investigate the response and reliability of the device for clinically acceptable flow ranges. The flow rate of the MPs impacts the trapping rate, as shown in Figure 7(b). The trapping rate is calculated by evaluating the total number of the trapped particles as a function of time. The lower wall of the channel is subjected to a higher magnetic field and force, which is used as the trapping line in the calculation of the trapping rate. In calculation, 6 particles are released after every 0.1 s for a longer duration of 100 s to maintain a similar flow environment to the experiment. The number of trapped particles increases over an evaluation time range from 0 to 100 s for the flow rates varying from 9 μl/min to 27 μl/min. In starting time (up to 20 s) of the simulation, all the flow rates Q (9 μl/min - 27 μl/min) show an almost similar trend (Figure 7(b)). For evaluating trapping rate, two different time intervals, i.e., 30 - 40 s and 80 - 90 s are selected to investigate the particle agglomeration over time. For initial time interval (30-40s), the flow rate varying from 15 μl/min to 27 μl/min shows a similar increment in the no. of trapped particles, i.e., ~8 particles/s. Meanwhile, the minimum flow rate ($Q = 9$ μl/min) shows 16 particles/s over the same time interval. However, after t = 40 s, all the flow rates (Q) show a significant enhancement in the trapping rate, as demonstrated in Figure 7(b). As the flow rate diminishes {27, 21, 15, 9} μl/min, the trapping rate increases rapidly which is evaluated as {29, 21, 11, 10} particles/s, respectively, over 80 - 90 s time interval. From the parametric study, the maximum trapping rate occurs at $Q = 9$ μl/min, as the magnetic force strongly dominates over the drag force.

A comparative analysis of particle trapping locations is investigated by splitting the bottom wall of the microfluidic channel into 33 equal line segments. The number of trapped particles at each line segment is estimated using the global evaluation method for different flow rates. Upon varying the flow rate from 9 to 27 μl/min, the percentage distribution of trapped particles is varied concerning trapping positions (bottom wall of the channel), as shown in Figure 8. The result shows that 80-90% of particles are localized in a band around a certain region similar to Figure 4 (d-g), whereas 10% - 20% are dispersed at other locations.

D. Experimental Verification on Particle Trapping Location and Trapping Efficiency

A comparison between numerical and experimental studies at various flow rates is carried out to establish an intuitive understanding of the influence of the magnetic field and geometry on the trapping locations and trapping efficiency. Usually, experiments involving particle dynamics are not deterministic, regardless of the method employed. Hence, the experimental characterization is repeated four times to verify the phenomena of particle trapping in the proposed magnetophoretic device. It is also essential to determine the possible experimental uncertainties in the investigation, which is calculated based on the student's t-distribution by considering a 95% confidence interval. The mean value from four sets of the experimental data is used to compare the trapping locations of the MPs and efficiencies against the simulation results.

Figure 10 shows the snapshots of the particle trapping locations for all the flow rates using a CCD camera, and it is observed that the trapping location changes with the sample flow rates. The lower flow rate $Q = 9$ μl/min has four bands of MP trapping, whereas other flow rates $Q = 15$ μl/min, $Q = 21$ μl/min, $Q = 27$ μl/min have only two bands of MP trapping at various locations at the lower wall of the channel, which shows a similar trend as in the simulation (Figure 4(d-g)). Such a large distribution of the trapped MPs is developed due to the special arrangement of the patterned

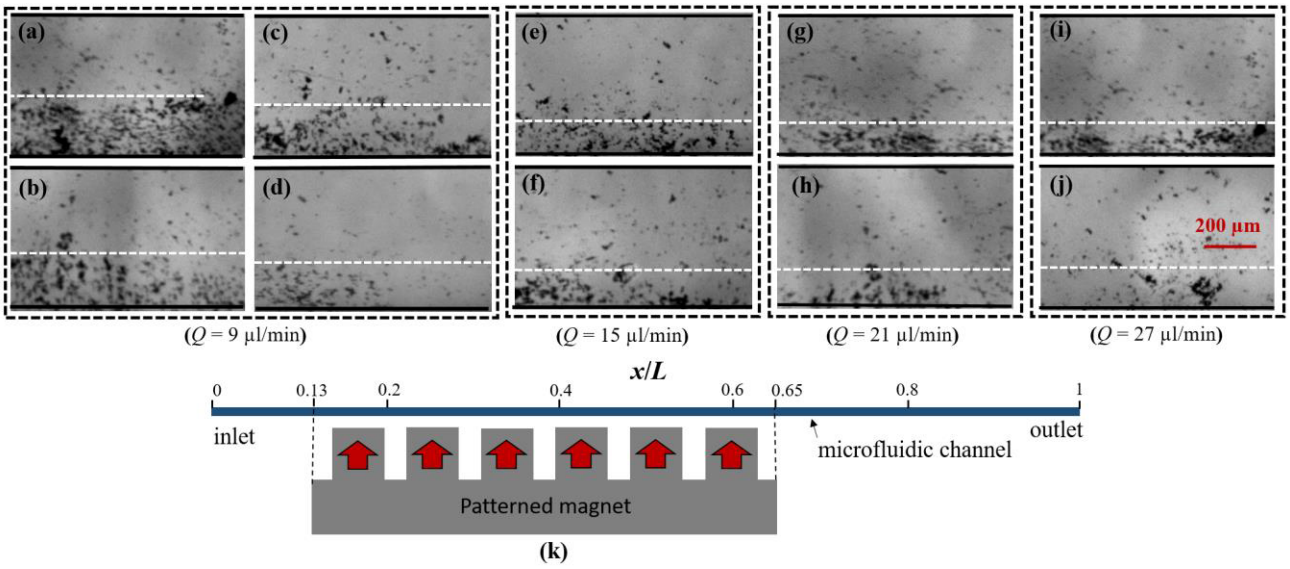

Fig. 10. Experimental investigation on the trapping of the MPs at the lower wall of the microfluidic channel in the presence of the magnetic field. The snapshot of the trapped MPs in a microfluidic chip for inlet flow rates (Q) (a-d) $Q = 9$ μl/min (e, f) $Q = 15$ μl/min (g, h) $Q = 21$ μl/min (i, j) $Q = 27$ μl/min at the location (a) $0.19 < x/L < 0.22$ (b) $0.34 < x/L < 0.37$ (c) $0.62 < x/L < 0.65$ (d) $0.71 < x/L < 0.74$ (e) $0.22 < x/L < 0.25$ (f) $0.56 < x/L < 0.59$ (g) $0.23 < x/L < 0.26$ (h) $0.71 < x/L < 0.74$ (i) $0.22 < x/L < 0.25$ (j) $0.70 < x/L < 0.73$ (k) Schematic representation of the device (not to scale), red arrow shows the magnetization direction of the patterned magnet.

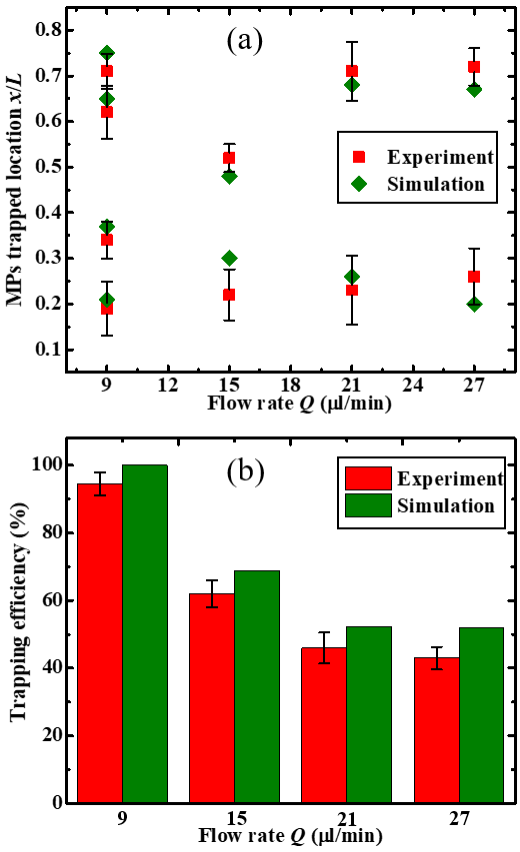

Fig. 11. Magnetic particle (a) trapping locations and (b) trapping efficiency at the lower wall of the microfluidic channel with different fluid flow rates $Q = 9$ μl/min, 15 μl/min, 21 μl/min, 27 μl/min.

magnet with the channel. With the change in the flow rate, the width of the MP trapping bands also changes, and the thicker bands are observed for the lower flow rates. The mean position

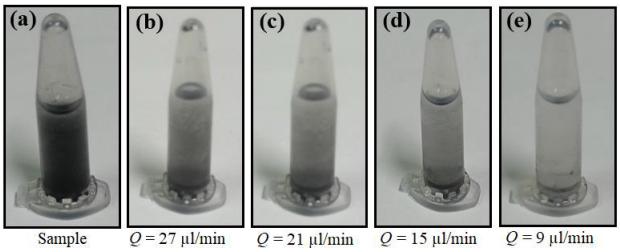

Fig. 12. (a) Injected sample at the inlet, (b-e) stored sample at the outlet for different flow rates 27-9 μl/min.

of the MP trapping bands from the simulation and experiment are used to validate the accuracy of the investigation, and the corresponding plot is shown in Figure 11(a). Four sets of experiment are performed for the flow rates of 9 μl/min - 27 μl/min to validate the simulated results, in which the volume of the sample at the inlet and outlet are stored in a jar, as shown in Figure 12 and the following formula is utilized for finding the trapping efficiency (TE).

$$TE = \frac{Vol_{at\ inlet} - Vol_{at\ outlet}}{Vol_{at\ inlet}} \tag{6}$$

The MP trapping efficiency with respect to flow rate for both experiment and simulation measurements are demonstrated and compared in Figure 11(b). For the FEM simulations, the trapping efficiencies of the MPs for different flow rates are evaluated using equation 5, which shows that the trapping efficiency decreases as the flow rate increases similar to the experiment. The uncertainty of the experimental trapping efficiency is determined for all the flow rates which varies from ± 3 to $\pm 5\%$, as depicted with the error bars in Figure 11(b). Maximum 94.6% and 100% trapping efficiencies are recorded for the lowest flow rate $Q = 9$ μl/min from experiment and simulation, respectively. A 5 to 7% difference between the numerical and experimental results is noted for various

TABLE II
COMPARATIVE STUDY ON MAGNETOPHORETIC TRAPPING IN CONTINUOUS FLOW MICROFLUIDIC CHANNEL

Source type [Ref.]	Particle type (size)	Fluid (flow rate)	Trapping efficiency
Coil based magnet [4]	Magnetic particle (1.4-8 μm)	Water (1 mm/s)	---
Bulk permanent Magnet [24]	DNA tagged magnetic bead (---)	Blood (40-120 μL/hr)	---
Permanent magnet [2]	E. coli labeled Magnetic bead (2 μm)	PBS (0.62-4 cm/s)	61.5%
Soft micromagnet [22]	Iron oxide particle (500nm)	Water (10 mm/s)	65%
Soft magnet with coil [1]	Magnetic bead (2.5μm)	Magnetic fluid (0.01-0.05 m/s)	80 %
Line magnetic dipole [3]	Magnetic bead (1 μm)	Non magnetic fluid (0.1-0.7 mm/s)	80 %
Patterned NdFeB magnet [This work]	Fe_3O_4 particle (0.5 μm)	DI water (9-27 μL/min)	94.6%

flow rates (9 μl/min to 27 μl/min), which shows a good agreement between the two approaches. Table II demonstrates the comparison of trapping efficiency of the present magnetophoresis device with other reported works. Due to patterning and integration of strong NdFeB powder based permanent magnet with the microfluidic channel, the reported device shows comparatively larger trapping efficiency at a clinically acceptable flow rate range. However, the trapping efficiency can be further improved by optimizing the gap between magnet and microfluidic channel or enhancing the intensity of magnetic field gradient.

V. CONCLUSION

In this work, a rapid fabrication technique of a robust, high-performance on-chip positive magnetophoretic system for manipulating magnetic particles is developed. The system consists of a high gradient thick patterned permanent magnet and microfluidic channel on a single PMMA substrate. A maximum 24 pN force is observed at the channel's lower wall due to the NdFeB patterned magnets. A FEM simulation model, including a magnetic field, laminar fluid flow, and particle tracing, is used to investigate the underlying physics for tracing the magnetic particles. Particle displacement from the upper wall for four flow rates, 9 μl/min, 15 μl/min, 21 μl/min, 27 μl/min, and corresponding particle distribution are discussed. The particle trapping rate and trapping efficiency are estimated for all the flow rates using the global evaluation method, leading to 100 % trapping efficiency for 9 μl/min in simulation, further verified experimentally with 94.6% efficiency. The reported results successfully demonstrate the proof-of-concept which can be further analyzed extensively to study the performance of the device using a variety of magnetically tagged biological samples to investigate the feasibility in case of real biological applications. Future work will focus on trapping biological entities like antibody-coated magnetic particle beads for targeting suitable antigens. Apart from the proposed biological applications, the reported results also show potential in a number of other areas such as in development of miniaturized water quality monitoring systems.

REFERENCES

[1] Y. Zhu, B. Zhang, J. Gu, and S. Li, "Magnetic beads separation characteristics of a microfluidic bioseparation chip based on magnetophoresis with lattice-distributed soft magnets," *J. Magn. Magn. Mater.*, vol. 501, May 2020, Art. no. 166485.

[2] Z. D. Call, C. S. Carrell, I. Jang, B. J. Geiss, D. S. Dandy, and C. S. Henry, "Paper-based pump-free magnetophoresis," *Anal. Methods*, vol. 12, no. 43, pp. 5177–5185, 2020.

[3] A. Samanta and N. Modak, "Influence of operating parameters in particle spreading, separation, and capturing in a hybrid free flow magnetophoretic bio-separator," *Phys. Fluids*, vol. 32, no. 11, Nov. 2020, Art. no. 112012.

[4] Q. Cao, Z. Li, Z. Wang, F. Qi, and X. Han, "Disaggregation and separation dynamics of magnetic particles in a microfluidic flow under an alternating gradient magnetic field," *J. Phys. D, Appl. Phys.*, vol. 51, no. 19, May 2018, Art. no. 195002.

[5] A. Munaz, M. J. A. Shiddiky, and N.-T. Nguyen, "Recent advances and current challenges in magnetophoresis based micro magnetofluidics," *Biomicrofluidics*, vol. 12, no. 3, May 2018, Art. no. 031501.

[6] P. Sajeesh and A. K. Sen, "Particle separation and sorting in microfluidic devices: A review," *Microfluidics Nanofluidics*, vol. 17, no. 1, pp. 1–52, Jul. 2014.

[7] F. Alnaimat, S. Karam, B. Mathew, and B. Mathew, "Magnetophoresis and microfluidics: A great union," *IEEE Nanotechnol. Mag.*, vol. 14, no. 3, pp. 24–41, Jun. 2020.

[8] S. Roy, D. Mallick, and K. Paul, "MEMS-based vibrational energy harvesting and conversion employing micro-/nano-magnetics," *IEEE Trans. Magn.*, vol. 55, no. 7, pp. 1–15, Jul. 2019.

[9] D. Mallick, K. Paul, T. Maity, and S. Roy, "Magnetic performances and switching behavior of co-rich CoPtP micro-magnets for applications in magnetic MEMS," *J. Appl. Phys.*, vol. 125, no. 2, Jan. 2019, Art. no. 023902.

[10] K. Paul, D. Mallick, and S. Roy, "Performance improvement of MEMS electromagnetic vibration energy harvester using optimized patterns of micromagnet arrays," *IEEE Magn. Lett.*, vol. 12, pp. 1–5, 2021.

[11] D. P. Arnold and N. Wang, "Permanent magnets for MEMS," *J. Microelectromech. Syst.*, vol. 18, no. 6, pp. 1255–1266, Dec. 2009.

[12] M. Hejazian and N.-T. Nguyen, "A rapid magnetofluidic micromixer using diluted ferrofluid," *Micromachines*, vol. 8, no. 2, p. 37, Jan. 2017.

[13] Y. Liu et al., "Label-free inertial-ferrohydrodynamic cell separation with high throughput and resolution," *Lab Chip*, vol. 21, no. 14, pp. 2738–2750, 2021.

[14] O. L. Lanier, C. Velez, D. P. Arnold, and J. Dobson, "Model of magnetic particle capture under physiological flow rates for cytokine removal during cardiopulmonary bypass," *IEEE Trans. Biomed. Eng.*, vol. 68, no. 4, pp. 1198–1207, Apr. 2021.

[15] S. A. Khashan, A. Alazzam, and E. P. Furlani, "Computational analysis of enhanced magnetic bioseparation in microfluidic systems with flow-invasive magnetic elements," *Sci. Rep.*, vol. 4, no. 1, p. 5299, May 2015.

[16] Q. Chen, D. Li, J. Lin, M. Wang, and X. Xuan, "Simultaneous separation and washing of nonmagnetic particles in an inertial ferrofluid/water coflow," *Anal. Chem.*, vol. 89, no. 12, pp. 6915–6920, Jun. 2017.

[17] Y. Liu et al., "Label-free ferrohydrodynamic separation of exosome-like nanoparticles," *Lab Chip*, vol. 20, no. 17, pp. 3187–3201, 2020.
[18] R. Zhou et al., "Fabrication and integration of microscale permanent magnets for particle separation in microfluidics," *Microfluidics Nanofluidics*, vol. 20, no. 7, p. 110, Jul. 2016.
[19] L. Zeng et al., "Label-free separation of nanoscale particles by an ultrahigh gradient magnetic field in a microfluidic device," *Nanoscale*, vol. 13, no. 7, pp. 4029–4037, 2021.
[20] F. Alnaimat et al., "Microfluidics based magnetophoresis: A review," *Chem. Rec.*, vol. 18, no. 11, pp. 1596–1612, 2018.
[21] H. Wang, S. Yamada, M. Matsuura, S. Sugimoto, and S. Tanaka, "Three-degree-of-freedom electromagnetic microactuator with powder-based Sm-Fe-N magnets and parylene beams," *J. Microelectromech. Syst.*, vol. 31, no. 4, pp. 634–643, Aug. 2022.
[22] E. P. Furlani and Y. Sahoo, "Analytical model for the magnetic field and force in a magnetophoretic microsystem," *J. Phys. D, Appl. Phys.*, vol. 39, no. 9, pp. 1724–1732, 2006.
[23] K. Y. Castillo-Torres, E. S. McLamore, and D. P. Arnold, "A high-throughput microfluidic magnetic separation (μFMS) platform for water quality monitoring," *Micromachines*, vol. 11, no. 1, p. 16, Dec. 2019.
[24] Y. Xu, Z. Zhang, Z. Su, X. Zhou, X. Han, and Q. Liu, "Continuous microfluidic purification of DNA using magnetophoresis," *Micromachines*, vol. 11, no. 2, p. 187, Feb. 2020.
[25] M. Golozar, M. Molki, and J. Darabi, "Computational and performance analysis of a continuous magnetophoretic bioseparation chip with alternating magnetic fields," *Microfluidics Nanofluidics*, vol. 21, no. 4, p. 73, Apr. 2017.
[26] M. T. Bodduluri, B. Gojdka, N. Wolff, L. Kienle, T. Lisec, and F. Lofink, "Investigation of wafer-level fabricated permanent micromagnets for MEMS," *Micromachines*, vol. 13, no. 5, p. 742, May 2022.
[27] Y. M. Patel, S. Jain, A. K. Singh, K. Khare, S. Ahlawat, and S. S. Bahga, "An inexpensive microfluidic device for three-dimensional hydrodynamic focusing in imaging flow cytometry," *Biomicrofluidics*, vol. 14, no. 6, Nov. 2020, Art. no. 064110.

Vinit Kumar Yadav (Student Member, IEEE) received the B.Tech. degree in electronics and communication engineering from the Pranveer Singh Institute of Technology, Kanpur, India, in 2015, and the M.Tech. degree in electronics and communication engineering from the National Institute of Technology Agartala, Tripura, India, in June 2019. Since December 2019, he has been a Ph.D. Scholar with IIT Delhi, India. His research interests include fabrication of permanent micromagnet for the application in MEMS and microfluidics, high-k dielectric materials growth by GLAD technique for nanoelectronics, and optoelectronics devices.

Yogesh M. Patel received the B.E. degree in mechanical engineering from Gujarat Technological University, India, in June 2016, and the M.Tech. degree in mechanical engineering from Nirma University, India, in June 2018. He has been a Full-Time Research Scholar with the Department of Mechanical Engineering, IIT Delhi, since July 2018. His research interests include the fabrication of microfluidic devices for cell analysis, imaging flow cytometry, hydrodynamic flow focusing, fluid mechanics, and heat transfer.

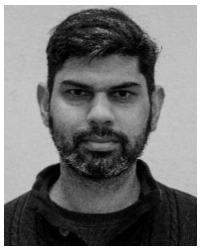

Supreet Singh Bahga received the B.Tech. degree in mechanical engineering from the IIT Bombay in 2007 and the M.S. and Ph.D. degrees in mechanical engineering from Stanford University, USA, in 2009 and 2013, respectively. He has been a Faculty Member with IIT Delhi, New Delhi, India, since 2013, where he is currently an Associate Professor with the Department of Mechanical Engineering. He is actively involved in experimental and computational research in microfluidics. He has authored over 40 articles in leading international journals and holds several patents to his credit.

Samaresh Das received the M.Sc. and Ph.D. degrees from IIT Kharagpur, India, in 2005 and 2011, respectively. He is currently an Associate Professor with the Centre for Applied Research in Electronics(CARE), IIT Delhi, India. His research interests include development of efficient infrared photodetectors, THz electronic devices, quantum information technology, and electronic biosensors.

Dhiman Mallick (Member, IEEE) received the Ph.D. degree in electrical and electronic engineering from the Tyndall National Institute, University College Cork, in 2017. He worked as Post-Doctoral Researcher at the Tyndall National Institute, Ireland for one and half years. He is currently an Assistant Professor with the Department of Electrical Engineering, IIT Delhi, India. He has authored around 63 published papers in peer-reviewed journals and conference proceedings, one book chapter, and one U.S. patent. His research interests include interdisciplinary microsystems engineering for autonomous sensor systems development.